Earthquake Research Advances 3 (2023) 100172

Contents lists available at ScienceDirect

Earthquake Research Advances

journal homepage: www.keaipublishing.com/en/journals/earthquake-research-advances

Rapid report of June 1, 2022 M_W 5.9 Lushan earthquake, China with geodetic and teleseismic data

Lei Xie [a], Nan Fang [b], Xiaoge Liu [b], Wenbin Xu [b,*]

[a] The Department of Land Surveying and Geo-Informatics, The Hong Kong Polytechnic University, Hong Kong, China
[b] Laboratory of Volcano and Earthquake Research, School of Geosciences and Info-physics, Central South University, China

ARTICLE INFO

Keywords:
Lushan earthquake
Near real-time deformation estimates
Rupture model
Dayi seismic gap

ABSTRACT

Timely response to earthquake characterization can facilitate earthquake emergency rescue and further scientific investigations. On June 1, 2022, M_W 5.9 earthquake occurred in the southern area of the Longmenshan fault zone. This event also happened at the south end of the Dayi seismic gap and is the largest earthquake that has occurred in this seismic gap since the 1970 M 6.2 event. The slip-distribution model constrained by the seismic waveforms suggests a thrust-dominated faulting mechanism. The main slip occurs at a depth of ~14 km, and the cumulative energy is released in the first 6 s. The variations of Coulomb stress caused by the mainshock show a positive change in the southwest area of the Dayi seismic gap, indicating possible activation of future earthquakes. In addition, we emphasize the importance of rapid estimation of deformation for near-field hazard delineation, especially when interferometric radar fails to image coseismic deformation in a high relief terrain.

1. Introduction

An earthquake of magnitude 5.9 struck Lushan County, Sichuan, China at 17:00 (UTC+8) local time on June 1, 2022. The China Earthquake Networks Center reported that the epicentre is located at 30.37° N, 102.94° E, which possibly represents an intraplate earthquake at Longmenshan (LMS) fault zone (Fig. 1). Due to the continued convergence between the eastern margins of the Qinghai-Tibetan Plateau and Sichuan Basin, the 2008 Wenchuan earthquake (M_W 7.9), 2013 Lushan earthquake (M_W 6.6), and 2017 Jiuzhaigou earthquake (M_W 6.5) also occurred in this distinct boundary fault system (Chen et al., 2013; Zheng et al., 2020). The 2022 earthquake is also felt at the south tip of the Dayi seismic gap after the 1970 Dayi Earthquake (M 6.2) with no recurrent events. The Mercalli intensity map released by China Earthquake Administration shows that more than 3 800 km^2 of the affected area can be subjected to at least the VI shaking level. The maximum NE-directed VIII shaking zone extends to ~70 km from the epicentre (https://www.cea.gov.cn/cea/xwzx/fzjzyw/5661356/index.html). As a result, several sections of highways in Baoxing and Lushan were temporarily cut off, and 135 houses were severely damaged (Xinhua News). A rapid search and rescue operation is underway, and more than 12,000 people have been relocated.

In this study, we present a rapid assessment of the characterization of the 2022 M_W 5.9 Lushan earthquake using seismic waveforms, Interferometric Synthetic Aperture Radar (InSAR) data, and near real-time deformation estimates. Tectonic setting, coseismic deformation prediction, slip and rupture model, and stress models are also documented to support emergency response and rescue operations. We also present the role of InSAR and deformation prediction software in the early post-seismic period and discuss the current stress perturbation in the Dayi seismic gap to support future investigations in this fold-and-belt area.

2. Tectonic setting and historical events

The 2022 Lushan earthquake occurred at the triple junction of Bayan Har block, Chuandian block, and South China block (Xu et al., 2013). The continuous compression and eastward extrusion of the Bayan Har block against the rigid South China block resulted in one of the most active

* Corresponding author.
E-mail address: wenbin.xu@csu.edu.cn (W. Xu).

Production and Hosting by Elsevier on behalf of KeAi

https://doi.org/10.1016/j.eqrea.2022.100172
Received 22 June 2022; Received in revised form 19 July 2022; Accepted 26 July 2022

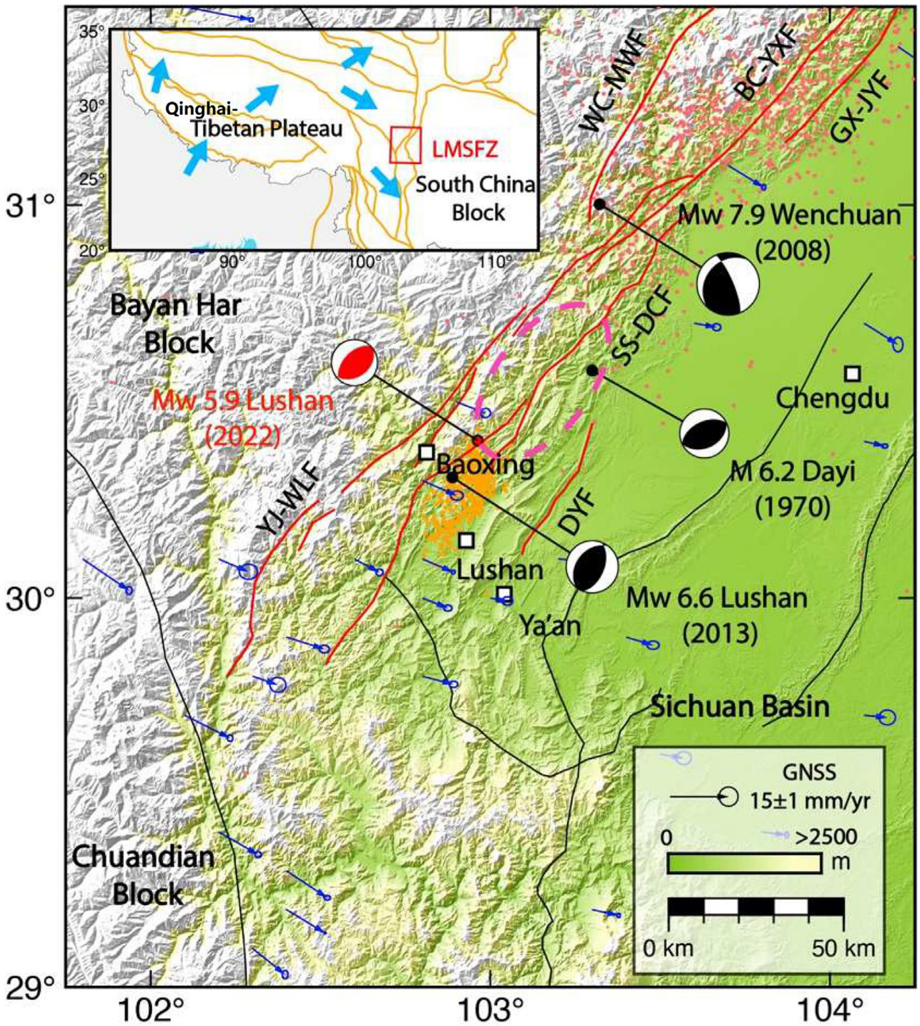

Fig. 1. Tectonic settings of the 2022 Lushan earthquake. The red lines indicate active faults within the LMS fault zone. The black lines indicate other faults. The dashed magenta ellipsoid represents the location of the Dayi seismic gap. The GNSS data are for both the campaigns and continuous sites from 1998 to 2014 (Zhao et al., 2015). The red and orange dots indicate the magnitude >3 aftershocks for the 2008 and 2013 events, respectively (Fang et al., 2015). The inset indicates the main faults (yellow lines) and motion of blocks (sky-blue arrows) around the Bayan Har block. (BC-YXF: Beichuan-Yingxiu Fault; DYF: Dayi Fault; GX-JYF: Guanxian-Jiangyou Fault; LMSFZ: Longmenshan Fault Zone; SS-DCF: Shuangshi-Dachuan Fault; WC-MWF: Wenchuan-Maowen Fault; YJ-WLF: Yanjing-Wulong Fault.)

intraplate convergent boundaries – the LMS fault system. The LMS fault system consists of a series of subparallel and north-east striking imbricated thrust faults that accommodate intense plate collisions between the eastern Tibet Plateau and Cratonic Sichuan Basin. These prevailing north-south trending faults, from north to south, can be classified as back-range faults (e.g., WC-MWF), central faults (e.g., BC-YXF), and mountain-frontal faults (e.g., SS-DCF), and range-front blind faults (e.g., DYF). Previous GNSS and levelling measurements indicate that the uplift rate is between 1 and 3 mm/yr (Liang et al., 2013; Wu et al., 2022). The fault slip rates constrained by the GNSS data and the geomorphological observations across the LMS fault zone are 2 ± 1 mm/yr and <1 mm/yr, respectively (Densmore et al., 2007; Rui and Stamps, 2016).

Spatially, the 2008 Wenchuan earthquake occurred on both the central and frontal faults in the northern and central areas of the LMS fault system, while the 2013 Lushan earthquake occurred in the southern counterpart and may have ruptured either the SS-DCF or its branch-fault (Xu et al., 2013). Between these two events, the aftershocks clearly delineate a seismically quiet area, namely the Dayi seismic gap, with a distance of 30–50 km along the ridges (Chen et al., 2013; Liu et al., 2018). From Coulomb stress analysis, historical earthquakes occurred on the LMS and Xianshuihe faults since the 1 700 s with the inter-seismic stress (1.3 kPa/yr) favoring future ruptures in the seismic gap, and the 1970 Dayi earthquake does not fully relieve the accumulated stresses (Guo et al., 2020; Liu et al., 2020; Liu et al., 2014a). The *in situ* borehole tests near Dachuan town (~20 km from the epicenter) also reveal that the SS-DCF is dominated by the NNW horizontal stress (Li et al., 2022). The maximum principal stress is comparable to the pre-seismic condition of the 2008 and 2013 events. However, the tomographic inversions of arrival times show a lower velocity zone beneath the seismic gap region, indicating a ductile deformation behavior and an unfavorable area to accumulate the stress. Therefore, the seismic gap may act as a barrier to the rupture propagation and very few aftershocks have been recorded. (Pei et al., 2015; Zheng et al., 2013).

Table 1
The USGS focal mechanisms estimated fault patch and slip for deformation simulations.

Nodal plane	Strike (°)	Dip (°)	Rake (°)	Depth (km)	Lon (°E)	Lat (°N)	M_W	Length (km)	Width (km)	Slip (m)
NP1	20	40	71	12	102.96	39.40	5.83	9.0	7.1	0.40
NP2	224	53	105							

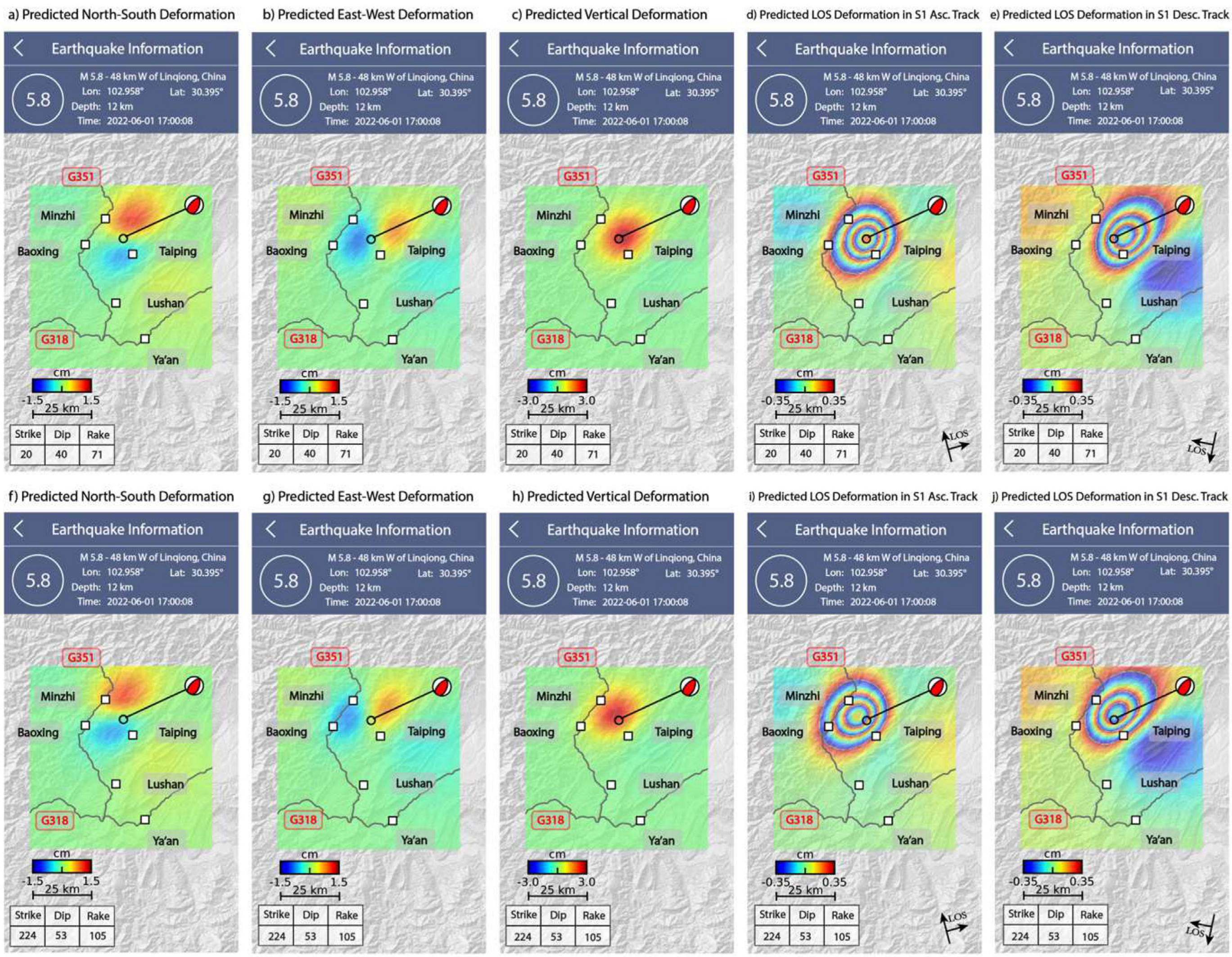

Fig. 2. Rapid deformation estimates from Codefmap.app. Nodal plane 1: a)–e); and Nodal plane 2: f)–j). The first column: North-South deformation; The second column: East-West deformation; The third column: Vertical deformation; The fourth and fifth columns: Line-of-sight (LOS) deformation in ascending (heading angle $\alpha \approx -10.6^\circ$, incident angle $\theta \approx 36.2^\circ$) and descending ($\alpha \approx -170.0^\circ$, $\theta \approx 42.7^\circ$) orbits, respectively.

3. Coseismic deformation

3.1. Rapid ground deformation prediction from Codefmap.app

We obtain the predicted three-dimensional coseismic deformation map using Codefmap.app (https://wenbin16.github.io/). This app was developed to rapidly generate coseismic deformation using United States Geological Survey (USGS) focal mechanism, rectangular dislocation model, and empirical slip formula in a near real-time manner (i.e., with a typical delay of 1 hr since the mainshock) (Ni and Xu, 2022). The app enables rapid and useful disaster assessment for InSAR users, decision-makers, and rescue teams. Here, the three-dimensional deformation estimates of the 2022 event are calculated based on the USGS focal mechanisms (Table 1). The slip (0.4 m) and rupture area (9.0 km × 7.1 km) are estimated from the scaling relations of moment magnitude (Blaser et al., 2010). Both nodal planes demote similar reverse-dominant motion and NE-SW orientation except in the dipping directions. The nodal plane 1 (NP1) with southeast-dipping fault geometry indicates a conjugate fault of the 2013 event, and better explains the aftershock distribution. The nodal plane 2 (NP2) with northwest-dipping shows a consistent fault geometry to the 2013 seismogenic fault plane (Jiang et al., 2014; Zhang et al., 2016). However, owing to the consistent thrust faulting and striking direction, the coseismic deformations estimated from two nodal plane solutions exhibit similar surface deformation patterns in all three components (Fig. 2). The simulated horizontal deformation displays three parallel lobe patterns, elongated NEE-SWW, and NW-SE in north-south and east-west directions, respectively. The simulated vertical deformation shows a maximum ~2.8 cm uplift of the NP1 and ~2.7 cm uplift of the NP2, surrounded by Minzhi, Baoxing, and Taiping (Fig. 2c and h). These simulated results suggest that the coseismic deformation is significant. The spaceborne data, especially the satellite radar data, might not easily capture the signal in the relief terrain. Ground-based measurements should be conducted to capture the coseismic signals. Regardless of different nodal plane solutions, a potentially hazardous zone bounded by the Baoxing, Minzhi, and Taiping can be identified, especially for the steep slopes along the G351 highway in the Minzhi-Baoxing section. Care should be taken during fieldwork in these regions and it is needful to be aware of secondary disasters (e.g., landslides).

3.2. InSAR observations

Based on the deformation prediction, we use two pairs of Sentinel-1 InSAR data acquired 4 and 9 days after the earthquake to map the surface deformation (ascending path 128: 20220529–20220610 and descending path 62: 20220524–20220605). Moreover, InSAR Scientific

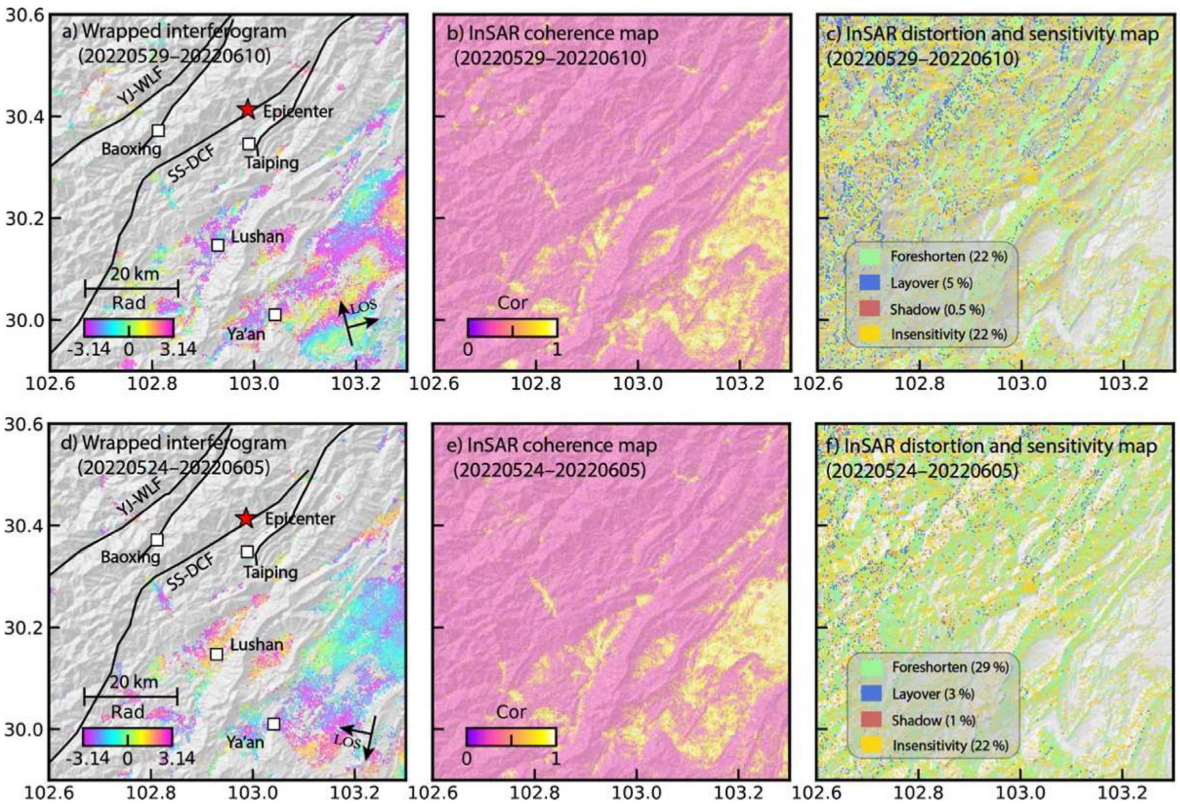

Fig. 3. Sentinel-1 coseismic observations. (a)–(c) Wrapped interferogram, coherence map, and distortion and sensitivity map for ascending track. (d)–(f) Similar subplots for descending track.

Computing Environment (ISCE) is used for interferometric processing (Rosen et al., 2012). The initial geometry-based co-registration is enhanced by the spectral diversity method to ensure subpixel accuracy (Fattahi et al., 2017). Furthermore, we use 1 arc-sec Shuttle Radar Topography Mission (SRTM) DEM to simulate and eliminate topographic phases (Farr et al., 2007). The 20:4 multi-look sampling and adaptive spectral filter are applied to improve the signal-to-noise ratio (Goldstein and Werner, 1998). However, the interferograms maintain coherence only in areas with relative flat topography and/or in urban areas with stable back-scattering features (Fig. 3). In the relief terrain, the side-looking radar geometry introduces geometric distortions (i.e., layover, foreshortening, and shadow) reducing InSAR visibility (Dun et al., 2021). For the area with layover and shadow, a useful echo signal is rarely seen. We find that 27.5% of the ascending pair area and 33.0% of the descending pair area are distorted according to the local incidence angle and topography (Fig. 3). The north-south trending slopes account for another 22% of insensitive areas due to the near-polar orbit of Synthetic Aperture Radar (SAR) satellites. Therefore, the near-field region loses its coherence even though spectral filters and multi-look operations are applied to suppress the noise. Compared with the 2013 event near Lushan (Liu et al., 2014b), the 2022 event occurred in a more steeply sloping region with dense vegetation coverage. No meaningful co-seismic deformation could be determined from Sentinel-1 observations in both orbits. As a result, we cannot use the Sentinel-1 interferograms to constrain the focal mechanism and reproduce the deformation patterns in this event.

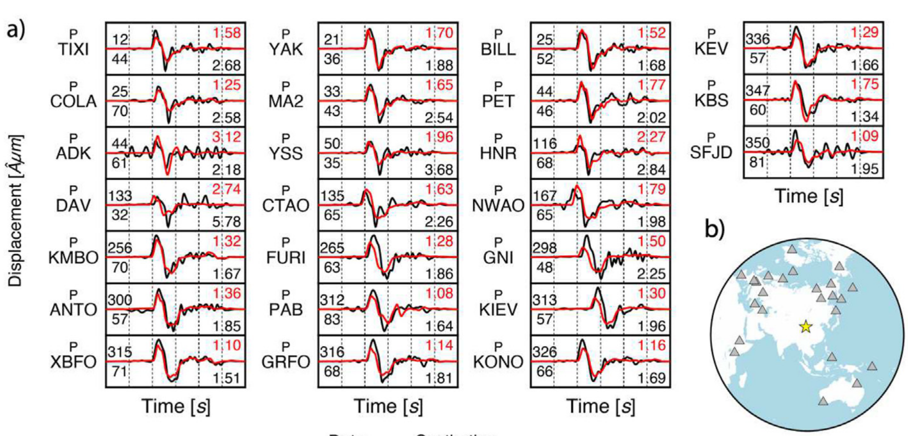

Fig. 4. The teleseismic P-wave records and synthetic waveforms. (a) The observed P-wave displacement (black) and inverted synthetic data (red). (b) The distribution of seismic stations.

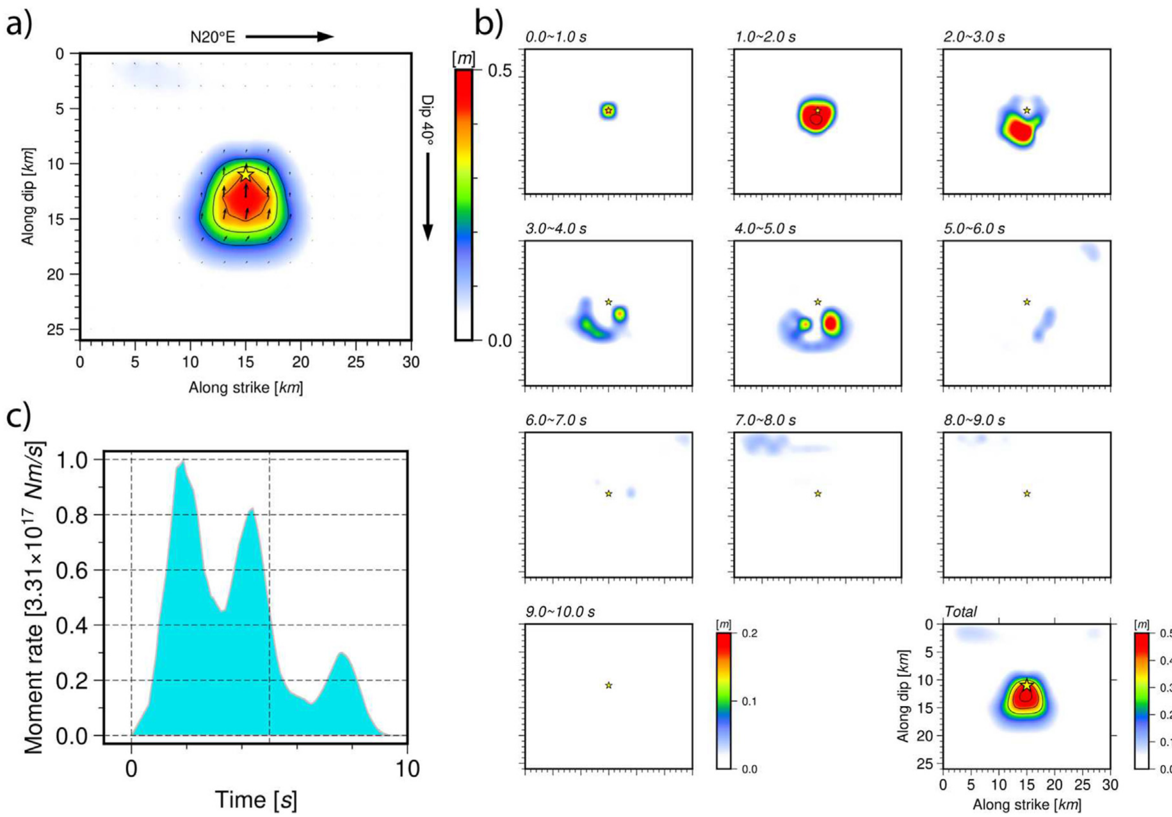

Fig. 5. Kinematic fault slip model. (a) The cumulative slip distribution model. The contour represents 0.1 m interval. (b) The propagation process of the rupture in 0–10 s. (c) The source time function of the earthquake.

4. Kinematic rupture slip model

We use broadband teleseismic P-waveform data from Incorporated Research Institutions for Seismology (IRIS) to invert for the dynamics of the rupture processes. We select 24 stations with homogeneous azimuthal distribution and a high signal-to-noise ratio at epicentral distances between 30° and 90° (Fig. 4b). The fault geometry is set up as the NP1 (Table 1): northeast-striking ($\varphi = 20°$) and southeast-dipping ($\delta = 40°$) plane for its better explanation of aftershock distributions. A 34 × 26 km fault plane is discretized into 2× 2 km patches. The P-wave recordings are filtered between 0.01 and 0.5 Hz after the removal of the instrument response (Fig. 4a). The slip distribution is then inverted using the non-negative least square method (Zheng et al., 2020). The resultant slip distribution reveals a thrust-dominated rupture concentrated on a 10 × 10 km asperity (Fig. 5a). The kinematics of ruptures begin at a depth of 12 km and progressively spread out to a depth of ~10–17 km (Fig. 5b). The substantial slip occurs during the first 6 s, with a maximum thrust of 0.5 m. The event releases a cumulative seismic moment of 1.2×10^{18} N m (equivalent to M_W 6.0).

5. Discussion

5.1. Codefmap.app vs. InSAR

Recent advancements in SAR satellite missions enable large coverage and high temporal-spatial resolution for rapid response to natural hazards (Li et al., 2021). The state-of-practice for InSAR observations in rescue and relief has been proven in many events, such as the 2022 Ms 6.9 Menyuan earthquake and the 2019 Ridgecrest earthquake sequence (Barnhart et al., 2019; Yang et al., 2022). However, taking the most widely used Sentinel-1 data as an example, it takes 4–6 h for the European Space Agency to release SAR data and restituted orbit. Another 0.5–1 h is needed for data collection, interferogram processing, and visualization. Therefore, under the most favorable conditions (i.e., the imaging time is immediately after the mainshock), 4–7 h are needed to get the interferometric products. Moreover, the influence of the decorrelation effect is an unavoidable problem in mountainous regions and can affect the interpretation of seismic interferograms. Although coherence is affected by several decorrelation factors such as thermal noise, geometric decorrelation, temporal decorrelation, and registration error (Lee and Liu, 2001), as we demonstrated in the Lushan area, geometric distortion is one of the primary factors in mountainous areas. In addition, for the C-band data, vegetation is another major obstacle that leads to random reflection signals even with 6–12 days of repeat orbits. In comparison, the Codefmap.app can provide timely surface deformation estimation after the earthquake occurrence. Generally, tens of minutes are needed for USGS to release the earthquake focal mechanisms from the teleseismic network. The server of Codefmap.app takes 1–2 min for the surface deformation estimation and data release. Typically, we should obtain the surface deformation simulation from user client on the smartphone in 1 h since the mainshock.

Therefore, the estimated surface deformation map can not only be used for investigating the fault properties but also provides an alternative and significant option for rescue-oriented purposes. Compared to other fast-sensing applications (e.g., Shakemap), Codefmap.app presents a more detailed coseismic surface motion in the near-field (Ni and Xu, 2022). Since the kinematic energy of only the seismic wave is sustained from seconds to minutes, secondary disaster (e.g., landslide, tsunami, building collapse) triggered by coseismic deformation is also critical for disaster response (Yue et al., 2020). Rapid deformation responses and seismic shaking make up for rescue time in the gold 72 h and can be applied before the real InSAR data are ready.

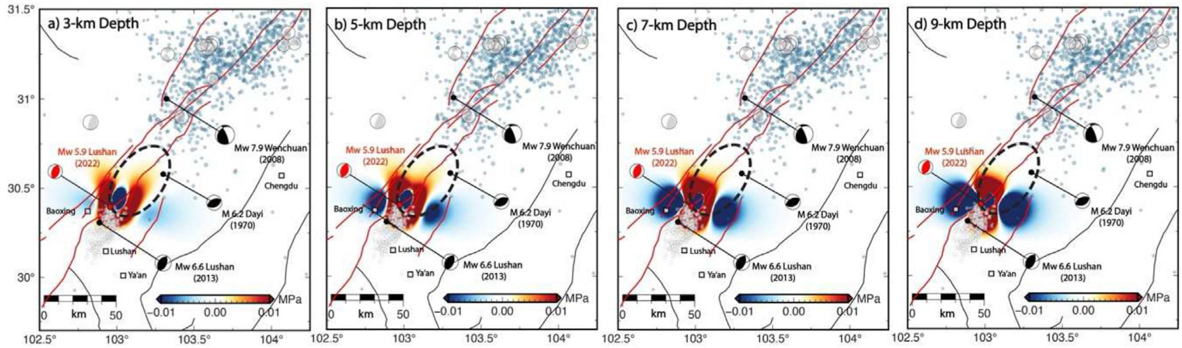

Fig. 6. Static ΔCFS at depths 3–9 km triggered by the 2022 M_W 5.9 Lushan earthquake. The red focal mechanism represents the USGS hypocenter of the 2022 Lushan earthquake. The dashed black ellipsoid represents the location of the Dayi seismic gap. The white and blue dots indicate the $3 < M < 5$ aftershocks for the 2008 and 2013 events, respectively. The grey focal mechanisms are M > 5 aftershocks.

5.2. *Effects of 2022 events on Dayi seismic gap*

Considering the 2022 Lushan earthquake, which occurred at the southwestern tip of the Dayi seismic gap, where no earthquake with a magnitude greater than 6 had occurred since the 1970 M 6.2 Dayi earthquake (Fig. 1), it is critical to assess the influence of the 2022 Lushan event on this earthquake gap. By utilizing the co-seismic slip model derived from teleseismic data as the driving source and assuming an effective coefficient $\mu = 0.4$, we estimate the changes in static Coulomb Failure Stress (ΔCFS) triggered by the 2022 event surrounding the Dayi seismic gap (Lin and Stein, 2004). Since the Dayi seismic gap is the transition zone between the Lushan earthquake and the Wenchuan earthquake, and the prevailing thrust and right-lateral slips of the LMS fault zone, we determine the receiver fault using the average of the 2008 and 2013 destructive events as strike = 208°, dip = 34°, and rake = 128° (Guo et al., 2020).

At the southwest section of the Dayi seismic gap, the static ΔCFS is consistently positive with a maximum of 0.1 MPa at different depths, excluding the short section in the central area (Fig. 6). The average ΔCFS value (~0.02 MPa) between 3 and 9 km depth within the gap is larger than the earthquake triggering threshold of 0.01 MPa (Hardebeck et al., 1998). Furthermore, this increased stress from the co-seismic slip expands across the YJ-WLF, which is the potentially responsible fault for the 2022 event. While the historical events along the LMS fault zone and Xianshuihe fault zone (between the 1700s and 2008) cast a stress shadow on the Dayi gap (~−100 kPa), the coseismic and postseismic (after-slip and viscoelastic relaxation) deformation transferred from Wenchuan and Lushan earthquake reverses the cumulative Coulomb stress along the YJ-WLF to a positive 30–50 kPa prior to the 2022 event (Guo et al., 2020; Liu et al., 2020). These findings suggest that the seismic hazard in the southwest Dayi seismic gap is further increased by the 2022 Lushan M_W 5.9 earthquake.

6. Conclusions

In this study, we present preliminary analyses of possible co-seismic deformation, fault slip model, and potential seismic hazards of the 2022 Mw 5.9 Lushan earthquake. The steep relief at the eastern boundary of the Tibet Plateau indeed poses significant challenges to the C-band Sentinel-1 interferograms, while the Codefmap.app shows an alternative near real-time deformation estimates and displays potentially hazardous areas near the Baoxing, Minzhi, and Taiping counties that might be helpful in rapidly evaluating the regional seismic hazards. The 2022 event is characterized as a thrust-dominated event with a maximum fault slip of 0.5 m and it increases the risk of potential seismic hazards in the southwest area of Dayi gap. Considering the accumulated stresses caused by historical strong earthquakes, we suggest a re-evaluation of seismic risk in the Dayi earthquake gap.

Declaration of competing interest

The authors declare that they have no known competing financial interests or personal relationships that could have appeared to influence the work reported in this paper.

Acknowledgement

The research is supported by the National Natural Science Foundation of China (No. 42174023). Seismic data are downloaded from IRIS data services (https://ds.iris.edu). Sentinel-1A data are from the ASF vertex (https://asf.alaska.edu). Coulomb-3 software is from USGS (https://www.usgs.gov/node/279387). Several figures were prepared by Generic Mapping Tools 6.0 (https://www.generic-mapping-tools.org).

References

Barnhart, W.D., Hayes, G.P., Wald, D.J., 2019. Global earthquake response with imaging geodesy: recent examples from the USGS NEIC. Rem. Sens. 11 (11), 1357. https://doi.org/10.3390/rs11111357.

Blaser, L., Kruger, F., Ohrnberger, M., Scherbaum, F., 2010. Scaling relations of earthquake source parameter estimates with special focus on subduction environment. Bull. Seismol. Soc. Am. 100 (6), 2914–2926. https://doi.org/10.1785/0120100111.

Chen, Y., Yang, Z., Zhang, Y., Liu, C., 2013. From 2008 Wenchuan earthquake to 2013 Lushan earthquake. Sci. Sin. Terrae 43 (6), 1064–1072. https://doi.org/10.1360/zd-2013-43-6-1064.

Densmore, A.L., Ellis, M.A., Li, Y., Zhou, R., Hancock, G.S., Richardson, N., 2007. Active tectonics of the Beichuan and Pengguan faults at the eastern margin of the Tibetan Plateau. Tectonics 26 (4). https://doi.org/10.1029/2006TC001987.

Dun, J., Feng, W., Yi, X., Zhang, G., Wu, M., 2021. Detection and mapping of active landslides before impoundment in the Baihetan reservoir area (China) based on the time-series InSAR method. Rem. Sens. 13 (16), 3213. https://doi.org/10.3390/rs13163213.

Fang, L., Wu, J., Wang, W., Du, W., Su, J., Wang, C., Yang, T., Cai, Y., 2015. Aftershock observation and analysis of the 2013 Ms 7.0 Lushan earthquake. Seismol. Res. Lett. 86 (4), 1135–1142. https://doi.org/10.1785/0220140186.

Farr, T.G., Rosen, P.A., Caro, E., Crippen, R., Duren, R., Hensley, S., Kobrick, M., Paller, M., Rodriguez, E., Roth, L., Seal, D., Shaffer, S., Shimada, J., Umland, J., Werner, M., Oskin, M., Burbank, D., Alsdorf, D., 2007. The shuttle radar topography mission. Rev. Geophys. 45 (2), RG2004. https://doi.org/10.1029/2005RG000183.

Fattahi, H., Agram, P., Simons, M., 2017. A network-based enhanced spectral diversity approach for TOPS time-series analysis. IEEE Trans. Geosci. Rem. Sens. 55 (2), 777–786. https://doi.org/10.1109/TGRS.2016.2614925.

Goldstein, R.M., Werner, C.L., 1998. Radar interferogram filtering for geophysical applications. Geophys. Res. Lett. 25 (21), 4035–4038. https://doi.org/10.1029/1998GL900033.

Guo, R., Zheng, Y., Xu, J., 2020. Stress modulation of the seismic gap between the 2008 Ms 8.0 Wenchuan earthquake and the 2013 Ms 7.0 Lushan earthquake and implications for seismic hazard. Geophys. J. Int. 221 (3), 2113–2125. https://doi.org/10.1093/gji/ggaa143.

Hardebeck, J.L., Nazareth, J.J., Hauksson, E., 1998. The static stress change triggering model: constraints from two southern California aftershock sequences. J. Geophys. Res. Solid Earth 103 (B10), 24427–24437. https://doi.org/10.1029/98JB00573.

Jiang, Z., Wang, M., Wang, Y., Wu, Y., Che, S., Shen, Z.-K., Bürgmann, R., Sun, J., Yang, Y., Liao, H., Li, Q., 2014. GPS constrained coseismic source and slip distribution of the 2013 Mw6.6 Lushan, China, earthquake and its tectonic implications. Geophys. Res. Lett. 41 (2), 407–413. https://doi.org/10.1002/2013GL058812.

Lee, H., Liu, J.G., 2001. Analysis of topographic decorrelation in SAR interferometry using ratio coherence imagery. IEEE Trans. Geosci. Rem. Sens. 39 (2), 223–232. https://doi.org/10.1109/36.905230.

Li, B., Xie, F., Huang, J., Xu, X., Guo, Q., Zhang, G., Xu, J., Wang, J., Jiang, D., Wang, J., Ding, L., 2022. In situ stress state and seismic hazard in the Dayi seismic gap of the Longmenshan thrust belt. Sci. China Earth Sci. 52, 1–10. https://doi.org/10.1007/s11430-021-9915-4.

Li, Y., Jiang, W., Zhang, J., Li, B., Yan, R., Wang, X., 2021. Sentinel-1 SAR-Based coseismic deformation monitoring service for rapid geodetic imaging of global earthquakes. Nat. Hazard Res. 1 (1), 11–19. https://doi.org/10.1016/j.nhres.2020.12.001.

Liang, S., Gan, W., Shen, C., Xiao, G., Liu, J., Chen, W., Ding, X., Zhou, D., 2013. Three-dimensional velocity field of present-day crustal motion of the Tibetan Plateau derived from GPS measurements. J. Geophys. Res. Solid Earth 118 (10), 5722–5732. https://doi.org/10.1002/2013JB010503.

Lin, J., Stein, R.S., 2004. Stress triggering in thrust and subduction earthquakes and stress interaction between the southern San Andreas and nearby thrust and strike-slip faults. J. Geophys. Res. Solid Earth 109 (B2). https://doi.org/10.1029/2003JB002607.

Liu, C., Dong, P., Zhu, B., Shi, Y., 2018. Stress shadow on the southwest portion of the Longmen Shan Fault impacted the 2008 Wenchuan Earthquake rupture. J. Geophys. Res. Solid Earth 123 (11), 9963–9981. https://doi.org/10.1029/2018JB015633.

Liu, Y., Wang, C., Shan, X., Zhang, G., Qu, C., 2014b. Result of SAR differential interferometry for the co-seismic deformation and source parameter of the MS7.0 Lushan Earthquake. Chin. J. Geophys. 57 (8), 2495–2506. https://doi.org/10.6038/cjg20140811 shu.

Liu, C., Zhu, B., Shi, Y., 2020. Do the two seismic gaps in the southwestern section of the Longmen Shan Fault present the same seismic hazard? J. Geophys. Res. Solid Earth 125 (3), e2019JB018160. https://doi.org/10.1029/2019JB018160.

Liu, M., Luo, G., Wang, H., 2014a. The 2013 Lushan earthquake in China tests hazard assessments. Seismol Res. Lett. 85 (1), 40–43. https://doi.org/10.1785/0220130117.

Ni, R., Xu, W., 2022. Codefmap APP: a seismic deformation simulation application based on Android system. Rev. Geophys. Planet. Phys. 53, 1–11. https://doi.org/10.19975/j.dqyxx.2022-037, 0.

Pei, S., Zhang, H., Su, J., Cui, Z., 2015. Ductile gap between the Wenchuan and Lushan earthquakes revealed from the two-dimensional Pg seismic tomography. Sci. Rep. 4 (1), 6489. https://doi.org/10.1038/srep06489.

Rosen, P.A., Gurrola, E., Sacco, G.F., Zebker, H., 2012, April 23. The InSAR Scientific Computing Environment. 9th European Conference on Synthetic Aperture Radar, Nuremberg, Germany.

Rui, X., Stamps, D.S., 2016. Present-day kinematics of the eastern Tibetan Plateau and Sichuan Basin: implications for lower crustal rheology. J. Geophys. Res. Solid Earth 121 (5), 3846–3866. https://doi.org/10.1002/2016JB012839.

Wu, Y., Zheng, Z., Nie, J., Chang, L., Su, G., Yin, H., Liang, H., Pang, Y., Chen, C., Jiang, Z., Bo, W., 2022. High-precision vertical movement and three-dimensional deformation pattern of the Tibetan Plateau. J. Geophys. Res. Solid Earth 127 (4), e2021JB023202. https://doi.org/10.1029/2021JB023202.

Xu, X., Wen, X., Han, Z., Chen, G., Li, C., Zhen, W., Zhang, S., Ren, Z., Xu, C., Tan, X., Wei, Z., Wang, M., Ren, J., He, Z., Liang, M., 2013. Lushan Ms 7.0 earthquake: a blind reserve-fault earthquake. China Sci. Bull. 58 (20), 1887–1893. https://doi.org/10.1007/s11434- 013-5999-4.

Yang, H., Wang, D., Guo, R., Xie, M., Zang, Y., Wang, Y., Yao, Q., Cheng, C., An, Y., Zhang, Y., 2022. Rapid report of the 8 January 2022 MS 6.9 menyuan earthquake, Qinghai, China. Earthq. Res. Adv. 2 (1), 100113. https://doi.org/10.1016/j.eqrea.2022.100113.

Yue, H., Zhang, Y., Ge, Z., Wang, T., Zhao, L., 2020. Resolving rupture processes of great earthquakes: reviews and perspective from fast response to joint inversion. Sci. China Earth Sci. 63 (4), 492–511. https://doi.org/10.1007/s11430-019-9549-1.

Zhang, G., Hetland, E.A., Shan, X., Vallée, M., Liu, Y., Zhang, Y., Qu, C., 2016. Triggered slip on a back reverse fault in the Mw6.8 2013 Lushan, China earthquake revealed by joint inversion of local strong motion accelerograms and geodetic measurements. Tectonophysics 672–673, 24–33. https://doi.org/10.1016/j.tecto.2016.01.031.

Zhao, B., Huang, Y., Zhang, C., Wang, W., Tan, K., Du, R., 2015. Crustal deformation on the Chinese mainland during 1998–2014 based on GPS data. Geodesy Geodyn. 6 (1), 7–15. https://doi.org/10.1016/j.geog.2014.12.006.

Zheng, A., Yu, X., Xu, W., Chen, X., Zhang, W., 2020. A hybrid source mechanism of the 2017 Mw 6.5 Jiuzhaigou earthquake revealed by the joint inversion of strong-motion, teleseismic and InSAR data. Tectonophysics 789, 228538. https://doi.org/10.1016/j.tecto.2020.228538.

Zheng, Y., Ge, C., Xie, Z., Yang, Y., Xiong, X., Hsu, H., 2013. Crustal and upper mantle structure and the deep seismogenic environment in the source regions of the Lushan earthquake and the Wenchuan earthquake. Sci. China Earth Sci. 56 (7), 1158–1168. https://doi.org/10.1007/s11430-013-4641-2.